ADVANCED MATERIALS TECHNOLOGIES
www.advmattechnol.de

Toward Printing the Brain: A Microstructural Ground Truth Phantom for MRI

Michael Woletz, Franziska Chalupa-Gantner, Benedikt Hager, Alexander Ricke, Siawoosh Mohammadi, Stefan Binder, Stefan Baudis, Aleksandr Ovsianikov, Christian Windischberger, and Zoltan Nagy*

Magnetic resonance imaging (MRI) has become the prime imaging technique for in vivo examination of the brain. In addition to anatomical and functional MRI, diffusion MRI (dMRI) is widely used in both clinics and research to assess tissue structure and fiber directions, particularly in the nervous system. While diffusion tensor imaging is the most widespread approach for assessing orientation measures, other, more sophisticated models have also been proposed. Validation of dMRI is, however, a challenging endeavor that requires specialized test samples. Here it is shown that two-photon polymerization (2PP) 3D printing allows for manufacturing such test objects, a.k.a. phantoms. After upscaling the 2PP fabrication process, 3D structures at high spatial resolution and sufficient size to image in a human 7T MRI scanner are created. These phantoms reliably mimic human white matter and thus enable the systematic validation and verification of dMRI data and their analyses. The 3D-printed structures include up to 51 000 microchannels that mimic the diffusion behavior of larger axons, with a cross-section of 12 × 12 µm^2 each, in parallel and crossing arrangements. The acquired dMRI data demonstrates and verifies the utility of these novel brain phantoms.

1. Introduction

Its non-invasiveness, versatility, and excellent contrast behavior make magnetic resonance imaging (MRI)[1] an important tool, without which modern healthcare cannot be imagined anymore. Nevertheless, MRI still has much more to offer. For example, diffusion imaging (dMRI),[2] is a high-potential modality, which exploits the directional variability of the water diffusion constant that results from the microstructural details of the local tissue. dMRI overcomes the resolution limits of conventional MRI and provides additional, clinically relevant data. Unfortunately, the complex biophysical processes that underlie the various contrast mechanisms make validating MRI results extremely challenging.

Although dMRI is widely used in research, the absence of reliable

M. Woletz, C. Windischberger
Division MR Physics, Center for Medical Physics and Biomedical Engineering
Medical University of Vienna
Vienna 1090, Austria

F. Chalupa-Gantner, S. Binder, A. Ovsianikov
3D Printing and Biofabrication Group
Institute of Materials Science and Technology
TU Wien
Vienna 1060, Austria
E-mail: franziska.gantner@tuwien.ac.at

F. Chalupa-Gantner, B. Hager, A. Ricke, S. Binder, S. Baudis, A. Ovsianikov
Austrian Cluster for Tissue Regeneration
Vienna 1200, Austria

B. Hager
High Field MR Centre
Department of Biomedical Imaging and Image-guided Therapy
Medical University of Vienna
Vienna 1090, Austria

A. Ricke, S. Baudis
Institute of Applied Synthetic Chemistry
TU Wien
Vienna 1060, Austria

S. Mohammadi
Department of Systems Neuroscience
University Medical Center Hamburg-Eppendorf
20249 Hamburg, Germany

S. Mohammadi
Department of Neurophysics
Max Planck Institute for Human Cognitive and Brain Sciences
04103 Leipzig, Germany

The ORCID identification number(s) for the author(s) of this article can be found under https://doi.org/10.1002/admt.202300176

DOI: 10.1002/admt.202300176

validation limits its utility in clinical settings considerably. This is particularly true for more advanced methods such as white matter (WM) tractography,[3,4] which aims to capture the 3D details of brain WM pathways.

The physical size of individual axons of the human brain WM, which ranges between 0.1 and 20 μm, is much too small to resolve with MRI. As such, MR tractography attempts to recreate the 3D undulating path of axon bundles rather than individual axons. Various methods exist for performing tractography on dMRI data. These may proceed in a deterministic manner by following e.g. the long axis of a diffusion tensor that can be fit to the dMRI data in each voxel[5,6] or rely on probabilistic methods.[7] However, without a chance for proper validation, it remains difficult to argue for or against the output of tractography pipelines. Further, the ever-increasing demand for reproducible research calls for methods and guidelines toward achieving much better reproducibility which has been demonstrated hitherto.[8,9]

Validation efforts require a "gold standard", but establishing such a gold standard is a complex endeavor that may run along various avenues. One way forward is to examine the same brain tissue sample with both dMRI and other well-established but more invasive methods. In this case, the results of the invasive method(s) are considered the gold standard.[10,11] There are obvious ethical limitations, safety concerns, and practical challenges to such invasive validation work, that necessitate another approach: designing and assembling inanimate test objects (a.k.a. phantoms). Given that the details of these phantoms can be adjusted by the experimenter and known with high precision a priori, they may be taken not only as a gold standard but even as the ground truth.[12]

Assembling such phantoms is challenging and they often either lack the complexity of in vivo tissue or their microstructural details are hard to control during the manufacturing process – or both. For example, even in areas of the brain WM, where axons had been conventionally considered to run "in parallel" and with a constant cross-sectional area, recent evidence indicates otherwise. Andersson et al. (2020) show that the individual axons subtend considerable angles to one another, have uniquely twisting paths and their cross-sectional area varies along their length.[13] These microstructural details are difficult to capture with phantoms that model WM with uniform straight cables or hollow tubes.[14,15] Other approaches produce more realistic microstructural details, but the resulting assembly is less well-known a priori.[16]

Here, we demonstrate that the high-resolution 3D printing technology[17] two-photon polymerization (2PP) (**Figure 1**) can be used to simultaneously overcome these shortcomings in manufacturing phantoms. With the help of additive manufacturing, new standards for the construction of 3D biomimetic scaffolds have been set.[18,19] The versatility of 2PP allows it to create objects with unprecedented precision and complexity while providing a high freedom of design.

2PP is a powerful tool within additive manufacturing domain that has become a state-of-the-art method for micro- and nanoscale fabrication with a wide range of applications.[18,20–22] 2PP takes advantage of the non-linear optical effect of two-photon absorption, which enables the fabrication of objects with features in the sub-micron region. However, the impressive spatial resolution comes at the cost of long fabrication times for larger objects.[23,24] Thus, the overall size of fabricated structures typically does not exceed few 100 μm in each dimension. Recent advances in the used hardware combined with upscaling strategies allows for a substantial increase in throughput,[25–28] thereby reaching the meso and macro scale while still providing high-resolution features.

In the present work, we optimize and utilize methods for producing upscaled 2PP-printed 3D phantoms with sufficient dimension for performing experiments in a 7T human MRI scanner. As a proof-of-principle, we design, print, and validate two phantoms with different arrangements of straight channels – one mimicking a parallel fiber arrangement, the other mimicking crossing axons. Besides the relatively large structure dimensions, the developed phantoms provide high densities of axon-mimicking microchannels with unprecedented aspect ratios.

The presented validation work includes tests that ascertain MRI compatibility of the printing material, check for artifacts, and uncover the actual fiber directions with tractography. Similar work in more complex phantoms that adhere more closely to actual microstructural details of in vivo fibers, such as curvatures or variation in density or diameter, is left for future efforts. After optimizing the 3D printing fabrication process and testing the produced structures, we present experimental evidence of the utility of our 3D-printed phantoms for MRI data and widely-used image processing pipelines.

2. Results and Discussion

2.1. Upscaled 2PP Fabrication

To overcome the limitations of conventional 2PP and thereby produce large enough phantoms for MRI, the fabrication process was upscaled in all three dimensions by combining two upscaling techniques (**Figure 2**a,b). First, the structure height is limited by the working distance of the objective (i.e., the distance from the front lens element of the objective to the focal point). To overcome this limitation, upscaling in z-direction was realized by mounting a material vat on the objective and dipping a structure holder into the vat. The structures were produced layer by layer on the sample holder, and the objective was moved downward after each written single voxel layer. Using this technique, the focal spot is kept at the same depth in the material, avoiding optical aberrations and a limitation of the achievable structure height, as described by Obata et al.[29] Second, the structuring area in xy-direction is limited by the field of view (FOV) given by the optical components. Structuring single building blocks in separate FOVs consecutively with a block height in z-direction of 300 μm and a xz-stitching angle of 12°

Z. Nagy
Max Planck Research Group MR Physics
Max Planck Institute for Human Development
14195 Berlin, Germany
S. Mohammadi
Laboratory for Social and Neural Systems Research (SNS Lab)
University of Zurich
Zurich8091, Switzerland

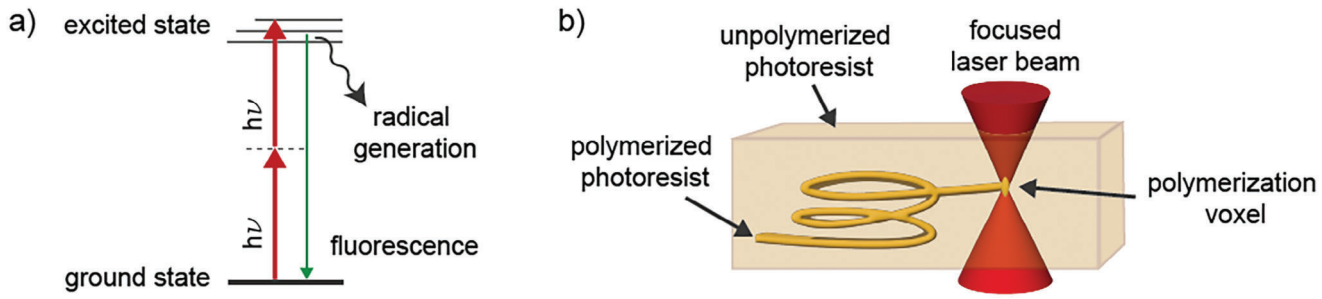

Figure 1. Principle of 2PP 3D Printing. a) Two photons are simultaneously absorbed by a photo-initiator molecule. Here *h* is Planck's constant and *ν* is the frequency of the laser light, hence their product provides the energy of each photon. From the excited state, the molecule can either emit a photon (fluorescence) or relax via intersystem crossing into a triplet state. From this triplet state, the molecule can create radicals that induce polymerization. b) Due to its low probability, two-photon absorption and subsequently polymerization of the photoresist occur only in a narrow area around the laser focus (polymerization voxel). The size of the polymerization voxel depends on the optical setup, material, and structuring parameters. 3D structures can be built with very high spatial and temporal control by moving the laser focus through the photoresist.

was found to be a fabrication strategy that allowed for upscaling in xy-direction (Figure S1, Supporting Information). With these upscaling methods, we were able to produce phantoms with dimensions of up to $7 \times 7 \times 4.2$ mm^3 and containing up to 51 000 microchannels.

2.1.1. Microchannel-Design Optimization and Validation

Before fabricating the final brain phantoms, the microchannels' fabrication, resolution, and design were optimized and validated regarding achievable channel cross-section, density, and infusibility (see Supporting Information). High channel densities are required to both appropriately mimic in vivo WM brain tissue and thus provide the expected diffusion weighting to the MRI signal as well as to increase the signal-per-volume ratio and provide an adequate signal amplitude for the measurements. Phantoms were designed to have channels with a cross-section of 12×12 μm^2 and a distance between the channels of 5 μm in horizontal and 12 μm in vertical direction (Figures S2 and S3, Supporting Information). The printing process had to be optimized and validated to maintain the quality of channel features in the upscaled 2PP structures. The size of the polymerization voxel depends on various factors, such as the numerical aperture of the objective, material reactivity, and the structuring power, and has a great impact on the achievable layer spacing and feature size. The polymerization voxel size can be increased by fabricating with higher laser powers, which enables structures with increased layer spacing and reduces the number of layers, thereby speeding up the fabrication process considerably. However, increasing polymerization voxel size and layer spacing reduces the achievable feature size and, subsequently, the overall quality of the structure. To optimize the 2PP processing in terms of structuring power, layer spacing, throughput, structure quality, and design, several test structures with parallel microchannels in one direction were printed and validated:

1) Test structures #1: The structures were fabricated to optimize layer spacing, structuring power, and throughput. A layer spacing of 5.5 μm at a structuring power of 70 mW was found to be an adequate compromise of structure quality and fabrication time (Figure 2c–e).
2) Test structures #2: The structures were designed to assess whether liquids could enter the individual channels of the xy-upscaled structures. After development, the structures were left in blue water-based dye to let the dye diffuse into the channels. Figure 2f shows the single layer of channels, imaged with an optical microscope, and confirming that the dye could diffuse into the channels. Further, test structures were immersed in fluorescent dye and imaged with laser scanning microscopy to prove that the walls between the channels were impermeable to water (Figure S4, Supporting Information).
3) Test structure #3: The structure was fabricated to assess whether microchannels were continuous over several stitching areas and writing blocks and whether liquid could diffuse into the individual channels of the structure that was upscaled in both xy- and z-directions. Figure 2g shows that the channeled area (14 322 microchannels) was entirely diffused by the blue dye.

2.1.2. Brain Phantoms: Preparation and Validation

Based on the optimized upscaled 2PP processing and validated microchannel designs, two MRI brain phantoms were fabricated with different channel arrangements to mimic common microstructural arrangements of WM axons:

Sandwich Brain Phantom: Structure size ($6 \times 6 \times 3$ mm^3), parallel microchannels in three distinguished layers providing larger volumes with channels oriented in the same direction. Each layer was $5792 \times 6000 \times 996$ μm^3 (**Figure 3**a). Distances between adjacent microchannels were 5 μm in horizontal and 12 μm in vertical direction yielding 14 322 microchannels per layer and a total of 42.966 (or 2478 microchannels mm^{-2}). Channels in the second layer were oriented orthogonal to channels in the first and third layers.

Wafer Brain Phantom: Structure size ($7 \times 7 \times 4.2$ mm^3), rows of parallel microchannels with alternating orientation along the x- and y-direction, providing two diffusion directions in the same voxel volume. Volume traversed by microchannels was $5090 \times 7000 \times 4040$ μm^3 (Figure 3b). Distances between adjacent microchannels were 5 μm in horizontal and 12 μm in vertical direction, leading to 25 500 microchannels per direction and a

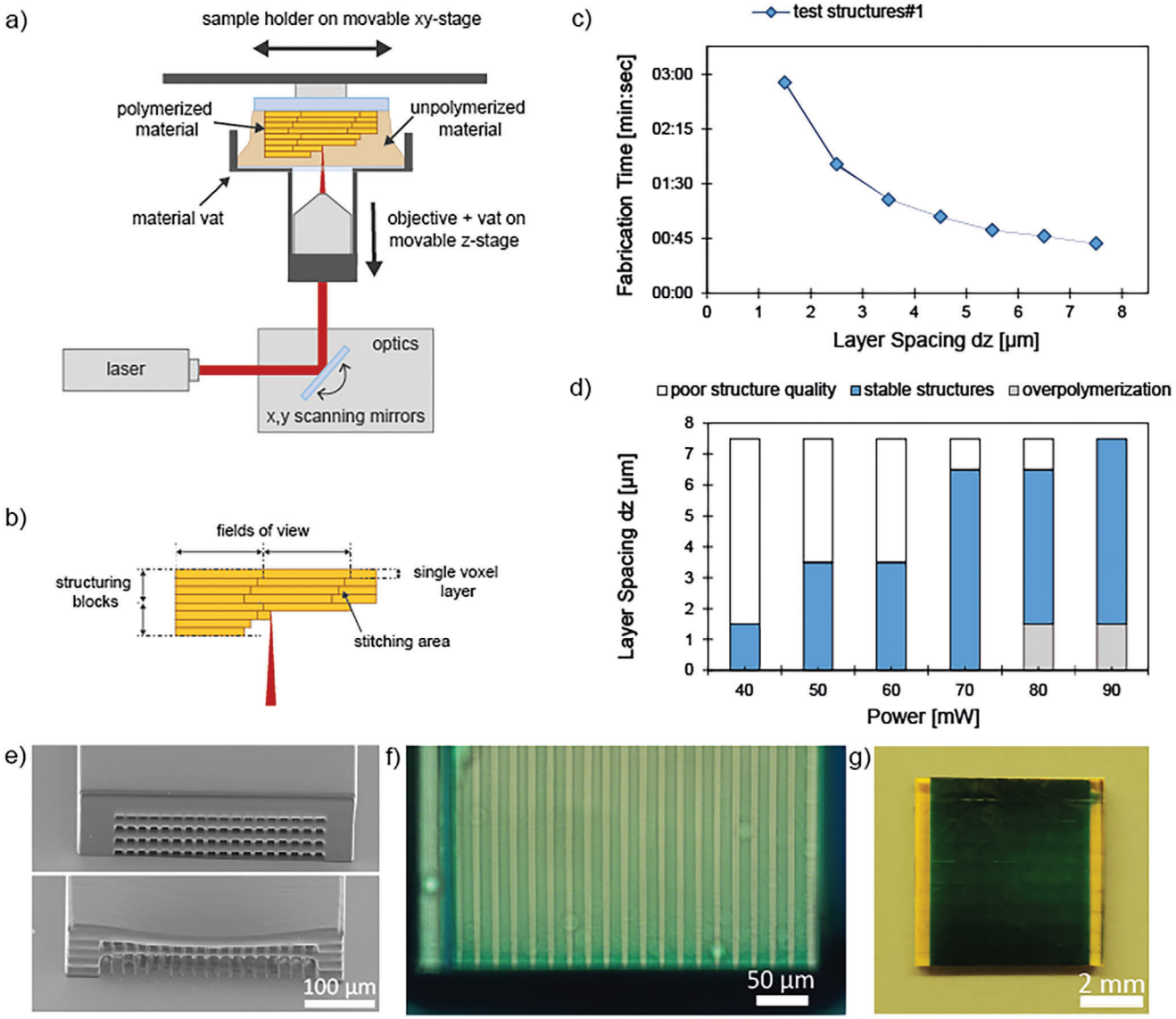

Figure 2. Upscaling, design optimization, and validation. a) Illustration of the upscaled printing process: A vat filled with photoreactive acrylic resin was mounted on the objective. The structure holder was dipped into the material and the objective was moved down after each printed layer in order to build the structures required. This setup ensured that the focal point was kept at a constant distance in the material. Smaller structuring blocks were built consecutively and stitched together in xy-direction. In the z-direction, blocks were fabricated on top of each other. b) Layout of upscaled structures. In each FOV, a block with a height of 300 µm was structured with single voxel layers. Blocks were stitched together at an angle of 12°. c) Fabrication time optimization: test structures #1 were printed with various layer spacings. The structuring time can be shortened significantly by increasing layer spacing, which comes at the cost of structure quality. d) Fabrication parameters were optimized by testing various settings for power and layer spacing in order to achieve optimal upscaled printing, increased throughput, and structure quality. e) Exemplary scanning electron microscopy images of test structures #1 during optimization of the printing process in terms of throughput and structure quality. Structures that were fabricated with 70 mW and a layer spacing of 5.5 µm showed excellent overall quality (top) while a layer spacing of 7.5 µm was insufficient and resulted in poor structure quality (bottom). f) Test structure #2 with a single layer of parallel channels (12 × 12 µm^2 cross-section) was infused with blue dye and imaged with an optical microscope to verify that the channels were free from non-polymerized material and open throughout the whole length of the structures. g) Test structure #3 with parallel channels in one direction. The dye diffused into the channels throughout the length of the phantom showing a clear difference between the colored porous areas and the edge area (yellow) that contains no channels.

total of 51 000 (or 2478 microchannels mm^{-2}). Figure 3c shows a cross-sectional scanning electron microscopy image of the channel arrangement used for the "sandwich" brain phantom.

For successful MRI imaging, two important features are required, MRI-visibility and the absence of susceptibility-related artifacts. For example, solids, such as bone and hard plastics, cannot be imaged with conventional MRI protocols as their MR signals have very short relaxation times and thus vanish before they can be acquired. Furthermore, due to differences in the magnetic susceptibility between the object itself and its surround-

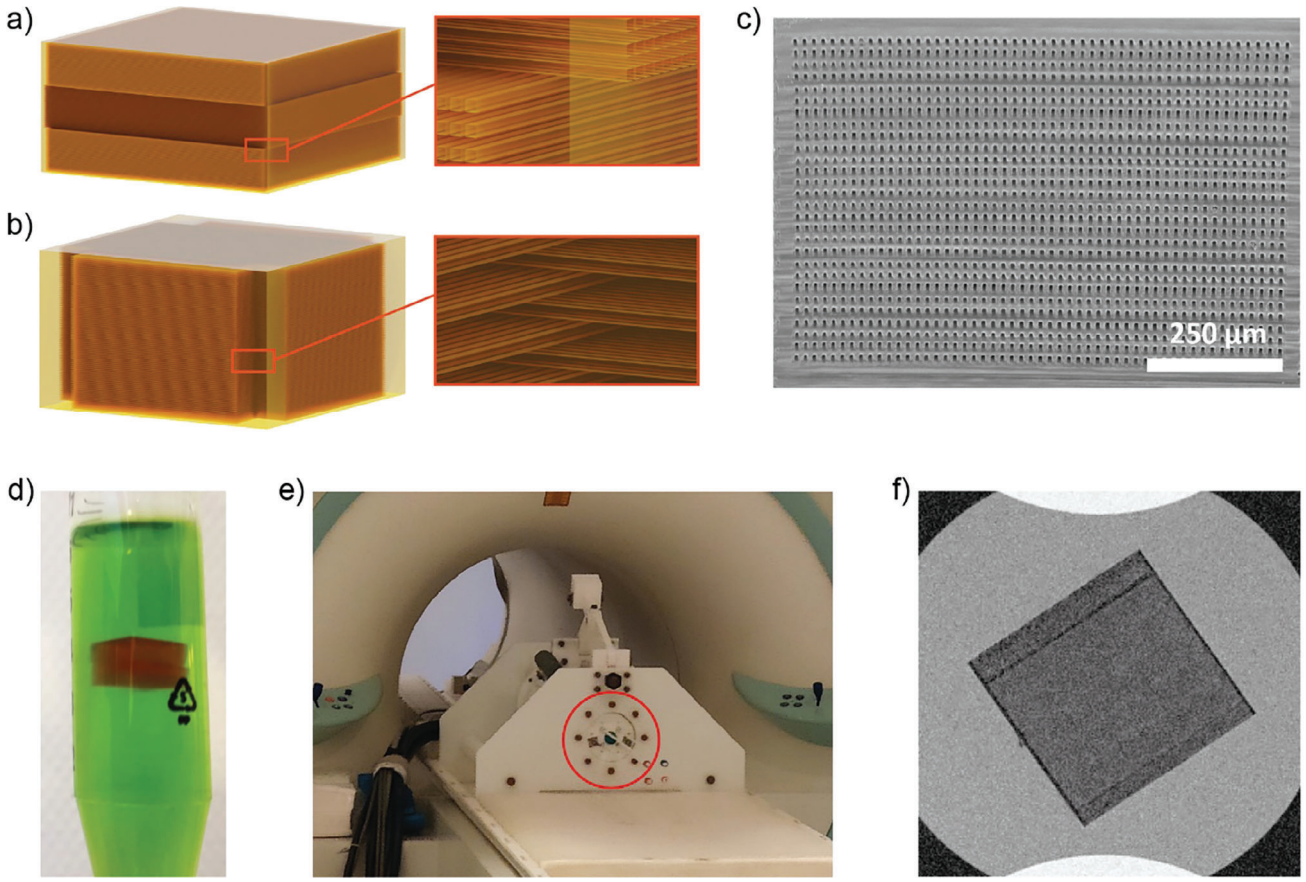

Figure 3. Phantom designs and validation. Schematic representation of the channel configurations of a) the sandwich (6 x 6 x 3 mm^3) and b) the wafer (7 x 7 x 4.2 mm^3) brain phantom. c) Scanning electron microscopy image of the channel configuration and density of the sandwich phantom. d) Phantom embedded in a gelatin-PBS mixture for subsequent MRI measurements. e) MRI measurements were performed at 7T with an MR microscopy gradient inset within a 19 mm volume resonator. The sample position is marked with a red circle. f) Brain phantom morphology measurements. T2-weighted MR images show that the phantom is MRI-compatible and MRI-visible. Further, they confirm that the phantom has a homogeneous appearance, except for a small linear inhomogeneity along the stitching area.

ings, local magnetic field gradients may arise, causing distortions, signal dropouts via intra-voxel dephasing, and other artifacts. In order to verify that the phantom manufactured in this study could be imaged correctly, phantoms were embedded in gelatin (Figure 3d) and placed into a 19 mm volume resonator within an MR microscopy gradient insert of a human 7T scanner (Figure 3e). Morphological MRI measurements showed that the phantom was clearly visible in its surroundings without image artifacts, confirming MRI compatibility and visibility (Figure 3f).

2.2. Diffusion MRI Measurements

Figure 4 details the proof-of-principle experimental results from the 3D-printed sandwich and wafer diffusion phantoms. Voxel-wise analysis via the ball-and-stick model[7] correctly identified the principal direction of water diffusion with high precision within the perpendicularly oriented channels in the separate layers of the sandwich phantom. Similarly, the presence of an alternating arrangement of crossing channels in the wafer phantom was also clearly revealed. Notably, the slice thickness was smaller than the thickness of the sections of the sandwich phantom so that within the phantom each voxel contained only channels that had identical orientation. On the contrary, within the image slices of the wafer phantom, each voxel contained an approximately equal number of channels in two perpendicularly oriented directions.

Additionally, the sandwich phantom data were put through tractography analysis, which correctly identified the a priori design: tracts were found to be parallel within each layer and the orientation of fibers in layer 2 was perpendicular to the orientation of fibers in layers 1 and 3 (**Figure 5**). For quality control, the Structural Similarity Index Measure (SSIM) was computed from the images with reversed phase polarity and without diffusion weighting as 0.99 and 0.98 for the sandwich and wafer configurations respectively. In addition, we have calculated field shifts for the sandwich phantom yielding minimum/mean/maximum shifts of −22.1, −3.58, and 15.2 Hz, with a standard deviation of 6.29 Hz. At 7 Tesla, this SD relates to field changes of only 0.02 ppm. Taken together, these results clearly show that the new phantom causes minimal field inhomogeneities.

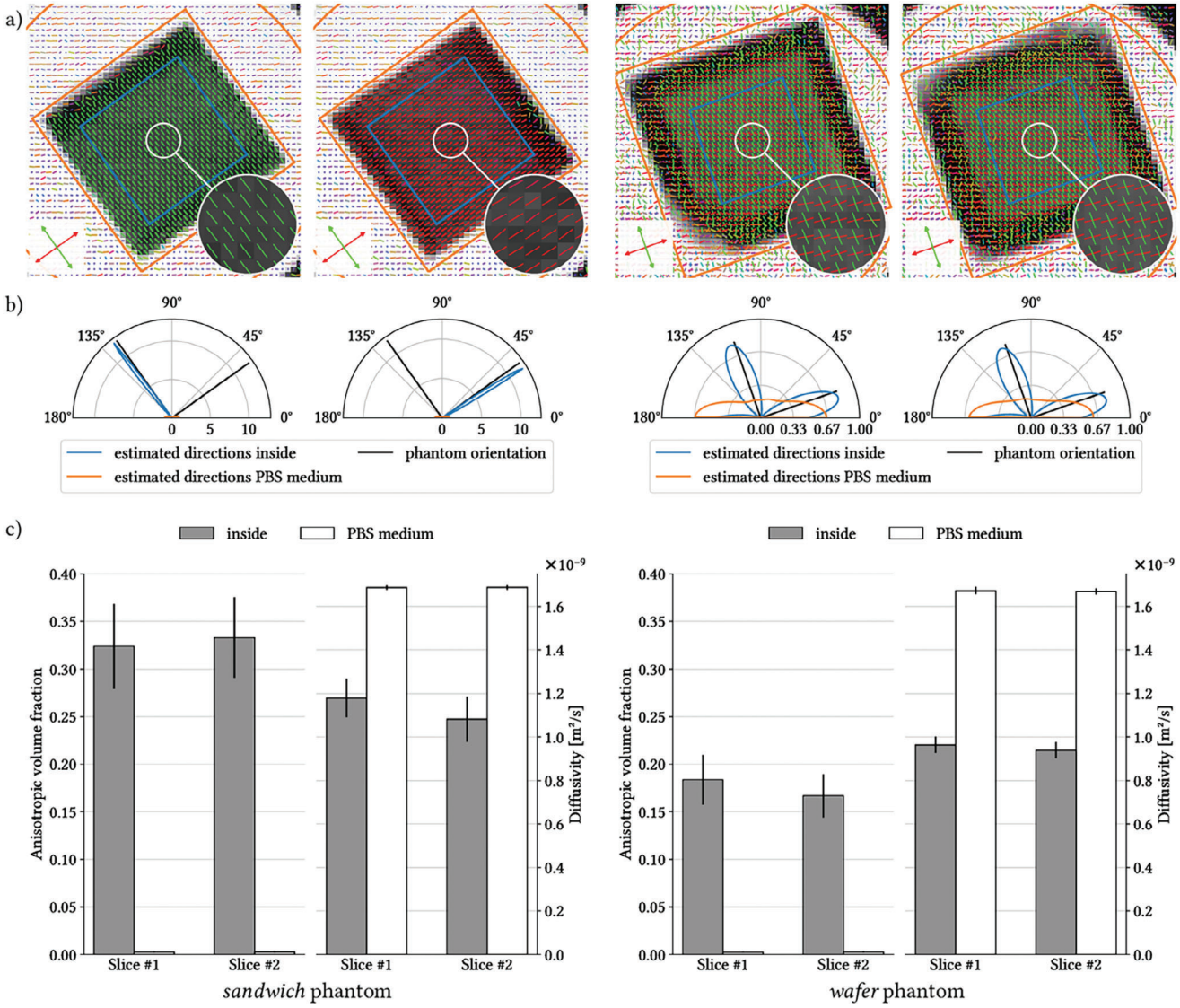

Figure 4. Validation of the phantoms for common dMRI measures. a) Voxel-wise analysis using a ball and sticks model correctly identified the direction of the channels running in unique perpendicular directions in separate sections of the sandwich phantom (left panels). For the wafer phantom where individual channel layer directions were interleaved (right panels), the channel crossing structure is clearly visible from the two estimated diffusion directions. b) Polar quantitative summary plots confirmed that channel orientation could be reliably reproduced in both the sandwich and the wafer phantom. The color coding of the measured directions corresponds to the masks as outlined in a), that is, inside the phantom (blue) and in the PBS medium (orange). c) Mean anisotropic volume fraction and mean diffusivity in the different slices and phantoms across voxels (error bars indicate the standard deviation across voxels). Analysis of the pure gelatin regions outside the phantom shows the expected absence of anisotropy and higher diffusivity.

3. Conclusion and Future Perspectives

We have successfully utilized a high-resolution 3D printing technique for manufacturing MRI-compatible objects with spatial dimensions that can be imaged in a human clinical MRI scanner and contain channels whose sizes approach the cross-sections of axons in the in vivo human brain. We validated these structures with common dMRI acquisition and data processing protocols, thereby demonstrating their utility as a ground truth phantom for developing and quality-assuring dMRI methods.

Attempts to create brain phantoms using 3D printing methods have been previously reported. However, those approaches used techniques that provide much lower printing resolutions, resulting in larger channel diameters that are more appropriate for mimicking muscle microstructure (e.g., Berry et al.[30] and Bieniosek et al.[31]) or for multiphasic, anthropomorphic phantoms (e.g., Kilian et al.[32]). So far, high-resolution stereolithography methods, such as 2PP 3D printing, were considered unsuitable for the production of an MRI brain phantom, due to the challenges in scalability.[12] Witherspoon et al.[33] recently introduced a ground-truth phantom fabricated with 2PP, which shows

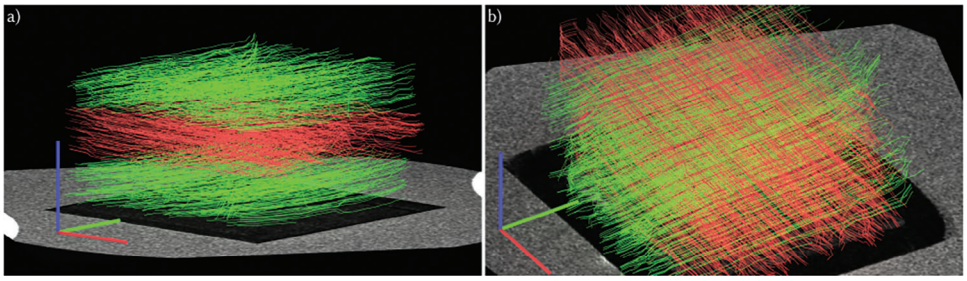

Figure 5. Tractography results of the a) sandwich and b) wafer phantom. The estimated fiber tracts reflect the design of the phantom with parallel arrangement within each layer and the mutually perpendicular orientation between adjacent layers for the sandwich phantom in (a) and the crossing arrangement for the wafer phantom in (b). Color-coding corresponds to the average direction of each individual estimated fiber and was aligned with the respective phantom's major axes.

the suitability of 2PP phantoms and demonstrates the opportunities that 2PP 3D printing provides for MRI phantom production. Their phantoms were, however, restricted in their length to 300 µm due to the fabrication process, and their microchannels were oriented in only one direction throughout the phantom. To create more complex and versatile phantoms that provide high aspect ratios and complex channel designs such as kissing or crossing fibers, sophisticated methods, some of which we present here, are needed to upscale 2PP 3D printing.

To this end, we utilized various techniques to speed up and upscale the 2PP printing process and were able to manufacture structures with an overall size of several mm^3 rather than $µm^3$ while still providing a high number and density of microchannels with a cross-section of 12 x 12 $µm^2$, making them suitable for mimicking larger axons.

In the present work, an acrylic resin was used for structuring since acrylates are known to produce highly cross-linked microstructures that simultaneously show good resolution and mechanical properties and are inert enough to withstand higher temperatures and harsh solvents.[34] Creating even larger and more complex phantoms with 2PP represents an important future challenge that requires a multi-faceted optimization effort. Despite the advancements in large-scale 2PP printing, creating high-volume structures remains difficult. Fabrication conditions and requirements regarding materials and designs require further scrutiny and improvement since materials can show shrinkage and signs of internal stress that might lead to cracks, deformation, or artifacts.

However, useful arrangements can be assembled from currently achievable printing sizes. **Figure 6** shows a rendering of our current design for a larger container that can house a number of smaller phantoms (i.e., similar dimensions as the sandwich and wafer designs in this study). The design also allows the individually customized orientation for each of the phantoms. With such an assembly it would be possible to investigate either different structures (i.e., different microstructural scenarios) in a single imaging experiment or to use the same phantom structure in all positions and orientations in the larger container to investigate how inherent limitations of the MRI scanner (e.g., gradient non-linearity resulting in a spatially variable b-value[35]) affect the results.

The brain phantoms we designed, manufactured, and tested herein contain only parallel channels. While this is a significant simplification of human brain tissue, it was necessary in order to establish the proof-of-principle and provide easily interpretable results. In vivo, WM is structured in a much more irregular manner. A significant advantage of using 3D printing for fabricating brain phantoms is the capability to change and adapt the channel configuration and thereby mimic brain WM more realistically. Therefore, a second avenue for improving on the presented results will be to fabricate and validate phantoms with high anatomical fidelity to specific microanatomical arrangements of axons. In both clinical practice and research, such phantoms are necessary and useful for determining the sensitivity and specificity

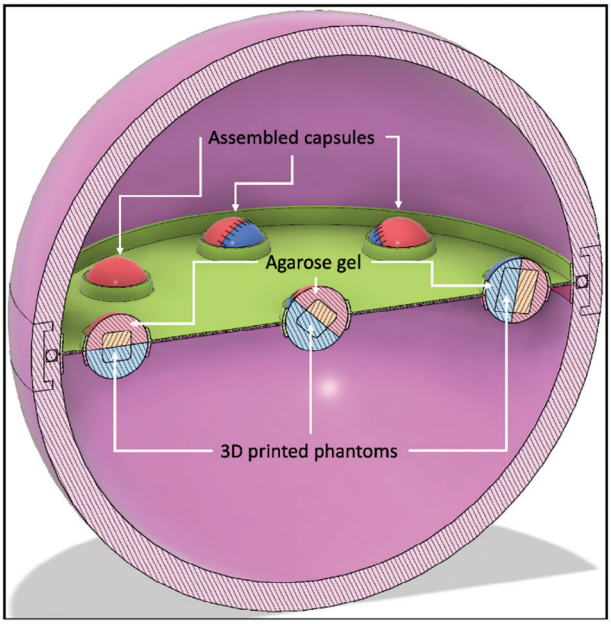

Figure 6. Rendering of a customizable phantom holder design. The assembly consists of a larger spherical shell (pink) into which a constellation of smaller capsules can be inserted in a layer (green). The layer is easily customizable to vary the number and position of the capsules (red/blue) and although only one of these layers is shown, more could be inserted as needed. Each capsule is filled with agarose gel and contains one 3D-printed phantom. Because the capsules are not permanently fixed to the holding layer, they can be rotated to any orientation. This facilitates experiments where copies of the same 3D printed phantom (e.g., wafer) could be positioned at different locations and orientations within the imaging volume of interest to investigate the effects of nonlinear gradients and, non-uniform transmit and receive RF fields on the image processing pipeline.

of imaging results for disease detection, investigating healthy tissue, and developing reliable image analysis methods. In particular, as 2PP can provide various arbitrary tract geometries with high precision, such phantoms would enable the validation of MRI-derived tractography results. More specifically, it would be possible to manufacture test objects tailored to the cardinal problem in tractography: differentiating crossing from touching ("kissing") fiber bundles. Consequently, the results of simulating diffusion processes could be directly compared to MRI data acquired from objects with the geometries used in simulations. Furthermore, different software packages for analyzing diffusion data can be evaluated and compared with respect to the underlying ground-truth geometry.

With validated tractography results, it will become possible to lay confidence in the detailed fiber structure information obtained from non-invasive in vivo diffusion imaging. This confidence will benefit the neuroscientific research of white matter microstructure. A subsequent positive impact can also be expected in clinical applications, where dMRI methods may expand from simple apparent diffusion coefficient mapping toward individualized fiber density quantification approaches. Reliable, validated mapping of fiber parameters and tracts will potentially also open up a new era of assessing psychiatric disorders based on changes in WM structure.

4. Experimental Section

Two-Photon Polymerization: For structuring, a 2PP setup was used, based on a tunable femtosecond NIR laser (80 MHz, 70 fs; MaiTai eHP DeepSee, Spectra-Physics) and a microscope objective (Super-Achromat 10x/0.4, Olympus). Printing was performed at 800 nm with a writing speed of 1000 mms^{-1}. The brain phantom structures were processed as computer-aided designs in the user software THINK 3D (UpNano GmbH) using the software cube designs, priority function, and for voxel compensation the "conservative" voxel mode. Structures were printed on glass coverslips that were mounted on a custom-made sample holder. To ensure attachment to the glass-surface, the sample holder was modified prior to the fabrication with methacrylate functionalities following a silanization procedure using 3-(Trimethoxysilylpropyl)-methacrylate (Sigma–Aldrich).[36]

Photoreactive Resin: A mixture was prepared at a weight ratio of 75:25 of ethoxylated trimethylolpropane triacrylate (ETA) (Sartomer 415) and trimethylolpropane triacrylate (TTA) (Genomer 1330), to which 5 $mmolg^{-1}$ of the photoinitiator M2CMK[37] was added. After fabrication, all structures were developed for several hours in 1-propanol (99.9% Sigma–Aldrich) to wash away unpolymerized material.

Printing Parameter Optimization:

(a) Test structures_1: 500 × 400 × 150 μm^3 with each structure fitting in a single FOV. The power was varied between 40 and 90 mW (steps of 10 mW), at layer-spacings from 1.5 to 7.5 µm (steps of 1 µm).

(b) Test structures_2: 400 × 6000 × 80 μm^3, traversed by a single layer of microchannels.

(c) Test structure_3: 6 × 6 × 1.5 mm^3, traversed by 14 322 channels in one direction.

Design Validation: For qualitative assessment of the fabrication process structures were imaged with a FEI Philips XL30 Scanning Electron Microscope. The samples were sputtered with a thin layer of gold before measurements. For imaging, structures were tilted by 45°. For optical microscopy inspection the channels were filled with blue food color (Dr. Oetker Back- und Speisefarben) diluted in water.

MRI Phantoms: In total two MRI phantoms were fabricated with optimized parameters (5.5 µm layer spacing, 70 mW structuring power), providing the sandwich and wafer design, and imaged in the MRI.

Preparation for MRI: After development, the brain phantoms were covered with phosphate buffered saline (PBS), left to degas in a vacuum chamber for several minutes, and then kept in the solution over night with a moving stirring bar, allowing the PBS to diffuse into the chanels. The brain phantoms were then embedded in an Eppendorf Tube in a mixture of PBS, 7% gelatin from porcine skin (Sigma, 175 g Bloom, Type A), and 0.05% sodium oxide to increase durability.

MRI Data Acquisition: All MRI data were collected on a Siemens 7T scanner (Magnetom, Siemens Healthineers, Erlangen, Germany) using a microimaging gradient insert (Resonance Research, Inc., Billerica, MA, USA) with a gradient strength of 750 mT m^{-1} and a 19-mm proton NMR volume coil (Rapid Biomedical, Würzburg, Germany). The scanning protocol included a T_2-weighted turbo-spin-echo sequence and a single-shot diffusion-prepared EPI sequence (CMRR multiband sequence[38]). The T_2-weighted image had TR/TE = 4 s/10 ms, 256 × 256 matrix size, 47 × 47 μm^2 in-plane pixel resolution and 400 µm slice thickness. The diffusion data had TR/TE = 4 s/32.2 ms, 72 × 72 matrix size, 208 × 208 μm^2 in-plane pixel resolution, b-values of 375, 875, 1375, and 1875 smm^{-2} and 64 diffusion directions per b-value and slice thickness of 800 µm versus 1.2 mm in the sandwich and wafer phantom respectively. The diffusion sequence was repeated with an inverted phase encoding direction. The dMRI data were analyzed with the help of FSL (https://fsl.fmrib.ox.ac.uk/) and MRtrix3 (https://www.mrtrix.org). The two datasets with opposing phase polarity were combined to increase the SNR and to alleviate distortions due to B_0 inhomogeneities using topup[39] in FSL. Similar to Witherspoon et al.,[33] the extend of B0 distortions was estimated by computing the structural similarity index measure (SSIM)[40] from the two images with opposing phase polarity within the phantoms. To identify the direction of the long axes of the channels in the 3D-printed phantoms, the distortion-corrected dMRI data were processed with bedpostx in FSL, that was, using a ball and stick model,[41] with a maximum of two independent directions per voxel. The mean outputs of bedpostx' Markov chain Monte Carlo (MCMC) fitting routine for the estimated fiber directions, as well as the estimated mean diffusivity and the volume fraction of the signals originating from each fiber in each voxel were reported and used for further analysis. As a proof-of-concept, the results from bedpostx were also used for fiber tracking, by applying the FACT algorithm[6] as implemented in MRtrix3[42] to the two estimated directions using two random seedpoints per voxel within a mask for each phantom, using an angular threshold of 45° and a stopping criterion of 5% of the anisotropic volume fraction.

Supporting Information

Supporting Information is available from the Wiley Online Library or from the author.

Acknowledgements

M.W. and F.C.-G. contributed equally to this work. The authors are grateful to Mr. Michael Kennedy for stimulating discussion and assistance with 3D modeling. The authors acknowledge TU Wien Bibliothek for financial support through its Open Access Funding Programme. ZN was financially supported by the Swiss National Science Foundation (grant nr: 31003A_166118). CW and MW were financially supported by the Austrian Science Foundation (FWF) and the Austrian Business Service (AWS). SM was supported by the German Research Foundation (DFG Priority Program 2041 "Computational Connectomics": MO 2397/5-1), by the Emmy Noether Stipend(MO 2397/4-1: MO 2397/4-2 : MO 2397/5-1 : MO 2397/5-2), and by the BMBF (01EW1711A and B) in the framework of ERA-NET NEURON.

Conflict of Interest

A patent describing the use of 3D printing for the creation of MRI phantoms was awarded (applicant: Technische Universität Wien; asignee: Medizinische Univeristät Wien; inventors: Aleksandr Ovsianikov, Peter Gruber, Christian Windischberger, Zoltan Nagy; US20220111581A1). Only three of the contributing authors of this publication are involved in the patent. A.O. is also a Co-Founder and CSO of UpNano GmbH, a recent spin-off of the TU Wien aiming at commercialization of 2PP.

Data Availability Statement

The data that support the findings of this study are available from the corresponding author upon reasonable request.

Keywords

brain phantoms, diffusion phantoms, diffusion-weighted MRI, high-resolution 3D printing, magnetic resonance imaging, microchannels, two-photon polymerization

Received: February 6, 2023
Revised: October 31, 2023
Published online:

[1] P. C. Lauterbur, *Nature* **1973**, *242*, 190.
[2] D. Le Bihan, *Nat. Rev. Neurosci.* **2003**, *4*, 469.
[3] S. N. Sotiropoulos, A. Zalesky, *NMR Biomed.* **2019**, *32*, e3752.
[4] K. H. Maier-Hein, *Nat. Commun.* **2017**, *8*, 1349.
[5] T. E. Conturo, N. F. Lori, T. S. Cull, E. Akbudak, A. Z. Snyder, J. S. Shimony, R. C. McKinstry, H. Burton, M. E. Raichle, *Proc. Natl. Acad. Sci. USA.* **1999**, *96*, 10422.
[6] S. Mori, B. J. Crain, V. P. Chacko, P. C. M. Van Zijl, *Ann. Neurol.* **1999**, *45*, 265.
[7] T. E. J. Behrens, M. W. Woolrich, M. Jenkinson, H. Johansen-Berg, R. G. Nunes, S. Clare, P. M. Matthews, J. M. Brady, S. M. Smith, *Magn. Reson. Med.* **2003**, *50*, 1077.
[8] T. E. Nichols, S. Das, S. B. Eickhoff, A. C. Evans, T. Glatard, M. Hanke, N. Kriegeskorte, M. P. Milham, R. A. Poldrack, J.-B. Poline, E. Proal, B. Thirion, D. C. Van Essen, T. White, B. T. T. Yeo, *Nat. Neurosci.* **2017**, *20*, 299.
[9] M. R. Munafò, B. A. Nosek, D. V. M. Bishop, K. S. Button, C. D. Chambers, N. Percie du Sert, U. Simonsohn, E.-J. Wagenmakers, J. J. Ware, J. P. A. Ioannidis, *Nat. Hum. Behav.* **2017**, *1*, 0021.
[10] S. Caspers, M. Axer, *NMR Biomed.* **2019**, *32*, e3779.
[11] T. B. Dyrby, G. M. Innocenti, M. Bech, H. Lundell, *NeuroImage* **2018**, *182*, 62.
[12] E. Fieremans, H. H. Lee, *NeuroImage* **2018**, *182*, 39.
[13] M. Andersson, H. M. Kjer, J. Rafael-Patino, A. Pacureanu, B. Pakkenberg, J. P. Thiran, M. Ptito, M. Bech, A. B. Dahl, V. A. Dahl, T. B. Dyrby, *Proc. Natl. Acad. Sci. USA.* **2020**, *117*, 33649.
[14] P. Pullens, A. Roebroeck, R. Goebel, *J. Magn. Reson. Imaging* **2010**, *32*, 482.
[15] C. Guise, M. M. Fernandes, J. M. Nóbrega, S. Pathak, W. Schneider, R. Fangueiro, *ACS Appl. Mater. Interfaces* **2016**, *8*, 29960.
[16] P. L. Hubbard, F. L. Zhou, S. J. Eichhorn, G. J. M. Parker, *Magn. Reson. Med.* **2015**, *73*, 299.
[17] J. Stampfl, A. Ovsianikov, L. Robert, *Multiphoton Lithography*, Wiley-VCH, Weinheim, Germany **2016**.
[18] T. Zandrini, S. Florczak, R. Levato, A. Ovsianikov, *Trends Biotechnol.* **2022**, *41*, 604.
[19] Y. Zhu, D. Joralmon, W. Shan, Y. Chen, J. Rong, H. Zhao, S. Xiao, X. Li, *Bio-Des. Manuf.* **2021**, *4*, 405.
[20] M. Carlotti, V. Mattoli, M. Carlotti, V. Mattoli, *Small* **2019**, *15*, 1902687.
[21] J. Song, C. Michas, C. S. Chen, A. E. White, M. W. Grinstaff, *Adv. Healthcare Mater.* **2019**, *9*, 1901217.
[22] S. O'halloran, A. Pandit, A. Heise, A. Kellett, *Adv. Sci.* **2022**, *10*, 2204072.
[23] X. Zhou, Y. Hou, J. Lin, *AIP Adv.* **2015**, *5*, 030701.
[24] F. Burmeister, S. Steenhusen, R. Houbertz, U. D. Zeitner, S. Nolte, A. Tünnermann, *J. Laser Appl.* **2012**, *24*, 042014.
[25] M. Malinauskas, V. Purlys, A. Žukauskas, M. Rutkauskas, P. Danilevičius, D. Paipulas, G. Bičkauskaite, L. Bukelskis, D. Baltriukiene, R. Širmenis, A. Gaidukevičiute, V. Bukelskiene, R. Gadonas, V. Sirvydis, A. Piskarskas, *AIP Conf. Proc.* **2010**, *1288*, 12.
[26] F. C. Wang, K. A. Wang, T. T. Chung, J. Y. Yen, *Adv. Mech. Eng.* **2017**, *9*, 1.
[27] S. K. Saha, D. Wang, V. H. Nguyen, Y. Chang, J. S. Oakdale, S. C. Chen, *Science* **2019**, *366*, 105.
[28] P. E. Petrochenko, J. Torgersen, P. Gruber, L. A. Hicks, J. Zheng, G. Kumar, R. J. Narayan, P. L. Goering, R. Liska, J. Stampfl, A. Ovsianikov, *Adv. Healthcare Mater.* **2015**, *4*, 739.
[29] K. Obata, A. El-Tamer, L. Koch, U. Hinze, B. N. Chichkov, *Light: Sci. Appl.* **2013**, *2*, e116.
[30] D. B. Berry, S. You, J. Warner, L. R. Frank, S. Chen, S. R. Ward, *Tissue Eng., Part A* **2017**, *23*, 980.
[31] M. F. Bieniosek, B. J. Lee, C. S. Levin, *Med. Phys.* **2015**, *42*, 5913.
[32] D. Kilian, W. Kilian, A. Troia, T.-D. Nguyen, B. Ittermann, L. Zilberti, M. Gelinsky, *ACS Appl. Mater. Interfaces* **2022**, *14*, 48397.
[33] V. J. Witherspoon, M. E. Komlosh, D. Benjamini, E. Özarslan, N. Lavrik, P. J. Basser, *bioRxiv* **2022**, 2022.
[34] C. N. LaFratta, J. T. Fourkas, T. Baldacchini, R. A. Farrer, *Angew. Chem., Int. Ed.* **2007**, *46*, 6238.
[35] Y. Lee, A. O. Kettinger, B. J. Wilm, R. Deichmann, N. Weiskopf, C. Lambert, K. P. Pruessmann, Z. Nagy, *Magn. Reson. Med.* **2020**, *83*, 2173.
[36] M. Lunzer, L. Shi, O. G. Andriotis, P. Gruber, M. Markovic, P. J. Thurner, D. Ossipov, R. Liska, A. Ovsianikov, *Angew. Chem., Int. Ed.* **2018**, *57*, 15122.
[37] A. Ajami, W. Husinsky, M. Tromayer, P. Gruber, R. Liska, A. Ovsianikov, *Appl. Phys. Lett.* **2017**, *111*, 071901.
[38] K. Setsompop, J. Cohen-Adad, B. A. Gagoski, T. Raij, A. Yendiki, B. Keil, V. J. Wedeen, L. L. Wald, *NeuroImage* **2012**, *63*, 569.
[39] J. L. R. Andersson, S. Skare, J. Ashburner, *NeuroImage* **2003**, *20*, 870.
[40] Z. Wang, A. C. Bovik, H. R. Sheikh, E. P. Simoncelli, *IEEE Trans. Image Process* **2004**, *13*, 600.
[41] S. Jbabdi, S. N. Sotiropoulos, A. M. Savio, M. Graña, T. E. J. Behrens, *Magn. Reson. Med.* **2012**, *68*, 1846.
[42] J.-D. Tournier, R. Smith, D. Raffelt, R. Tabbara, T. Dhollander, M. Pietsch, D. Christiaens, B. Jeurissen, C.-H. Yeh, A. Connelly, *NeuroImage* **2019**, *202*, 116137.